Numerical Diagnostics of the Electrostatic Potential Perturbed by Magnetic Islands

Seiya NISHIMURA, Naohiro KASUYA, Masatoshi YAGI[1,2], Kimitaka ITOH, Sanae-I. ITOH[1] and Nobuyoshi OHYABU

National Institute for Fusion Science, Gifu 509-5292, Japan
[1]*Research Institute for Applied Machanics, Kyushu University, Fukuoka 816-8580, Japan*
[2]*Japan Atomic Energy Agency, Ibaraki 311-0193, Japan*

(Received 7 December 2009 / Accepted 11 March 2010)

Nonlinear dynamics of a magnetic island is simulated using a set of reduced two-fluid equations, and the excitation of the electric field in the vicinity of the magnetic island is observed. An impact of the error field (external symmetry-breaking magnetic perturbation) on the electric field is examined, and its global structure changes with a small error field. A numerical measurement simulating the heavy ion beam probe is carried out on the field given by the nonlinear simulation. An effect of the finite width of the injected beam is taken into account, and the spatial resolution is evaluated. It is found that the measuring error due to the finite beam width is significant when the radial gradient scale length of the electrostatic potential is comparable to the beam width.

Keywords: magnetic island, electrostatic potential, numerical diagnostics, heavy ion beam probe, error field

DOI: 10.1585/pfr.5.S2057

1. Introduction

Control of magnetic islands is one of important issues for magnetically confined fusion plasmas [1]. In order to understand impacts of the magnetic island on the plasma confinement, experimental observations and numerical simulations have been done. In the Large Helical Device (LHD), which is an stellarator employing a heliotron magnetic field, the excitation of the radial electric field in the vicinity of the magnetic island has been observed [2]. In the numerical simulation of tokamak plasmas, the excitation of the radial electric field due to the magnetic island is also observed [3–5]. However, the detailed comparison among them has not been examined.

We have been developing a turbulence diagnostic simulator, in which the nonlinear dynamics of toroidal plasmas is simulated, and analyses similar to experimental measurements are carried out on numerical data. This idea is based on the previous achievement by the coupling of experimental observations and numerical simulations in a linear device [6, 7]. The simulator is available for comparing simulation results with experimental observations, and for the development of the data analysis technique.

In the present study, the nonlinear simulation data of the electrostatic potential perturbed by magnetic island is measured for showing how the locking of the island is observed by numerical heavy ion beam probe (HIBP). This paper is organized as follows. In Sec.2, we introduce our model equations and the nonlinear dynamics of the magnetic island is simulated. In Sec.3, the numerical diagnostics of the electrostatic potential near the island is carried out using the numerical HIBP module, where spatial resolution and error bar due to the beam width are evaluated. Sec.4 is devoted to a summary.

2. Numerical Simulation

2.1 Model

In this study, a large aspect ratio tokamak plasma is modeled by a cylindrical plasma with the periodic boundary in the toroidal direction. We assume the cold ion limit and the quasi-neutral condition between the ion density and the electron density. The parallel ion velocity and neoclassical effects are neglected, for simplicity. Under these conditions, we introduce reduced two-fluid equations derived from Braginskii's transport equations. The vorticity equation, the generalized Ohm's law, the continuity equation, and the electron heat balance equation (See Ref. [5] for details) are respectively given by

$$\frac{D}{Dt}\nabla_\perp^2\phi = \nabla_\parallel j_\parallel + \mu\nabla_\perp^4\phi, \tag{1}$$

$$\frac{\partial}{\partial t}A = -\nabla_\parallel(\phi - \delta p) - \eta_\parallel j_\parallel + \alpha_T\delta\nabla_\parallel T, \tag{2}$$

$$\frac{D}{Dt}n + \beta\frac{D}{Dt}p = \delta\beta\nabla_\parallel j_\parallel + \eta_\perp\beta\nabla_\perp^2 p, \tag{3}$$

$$\frac{3}{2}\frac{D}{Dt}T - \frac{D}{Dt}n = \alpha_T\delta\beta\nabla_\parallel j_\parallel + \epsilon^2\chi_\parallel\nabla_\parallel^2 T + \chi_\perp\nabla_\perp^2 T, \tag{4}$$

where $\alpha_T = 0.71$ for hydrogen plasmas. D/Dt is a convective derivative, in which the $E \times B$ drift is taken into

author's e-mail: nishimura.seiya@lhd.nifs.ac.jp

account. $\nabla_\perp^2$ is a Laplacian perpendicular to the perturbed magnetic field line, and $\nabla_\parallel$ is a vector operator parallel to the field line. The variables $\{\phi, A, n, T, p, j_\parallel\}$ indicate the electrostatic potential, the parallel vector potential, the electron density, the electron temperature, the electron pressure and the parallel electric current, respectively. Transport coefficients $\{\mu, \eta_\parallel, \eta_\perp, \chi_\parallel, \chi_\perp\}$ are the ion viscosity, the parallel resistivity, the perpendicular resistivity, the electron parallel thermal conductivity, and the electron perpendicular thermal conductivity, respectively. In the dissipationless limit, this system conserves the energy. $\epsilon = a/R_0$ is an inverse aspect ratio, where $\{a, R_0\}$ are a minor and major radii of plasma, respectively. δ is the ion skin depth normalized to the minor radius and β is a ratio between the kinetic pressure and the magnetic one measured at the plasma center. The time, the radial length and the toroidal length are normalized as $t/\tau_A \to t$, $r/a \to r$, $z/R_0 \to z$ with $\tau_A = R_0/v_A$, where v_A is the Alfvén velocity. Especially, the electrostatic potential is normalized as $\phi(c\tau_A/B_0a^2) \to \phi$, where $\{c, B_0\}$ are the velocity of the light and the ambient magnetic field.

2.2 Simulation parameters

For the numerical simulation, parabolic profiles are considered for the density and the electron temperature, and the safety factor defined by $1/q(r) = -(1/r)\mathrm{d}A_0/\mathrm{d}r$ is given by $q(r) = 1.5 + 0.5(r/r_s)^3$, where r_s is a radial position of the $q = 2$ resonant surface. Note that there does not exist the electrostatic potential in the initial state. In the numerical simulation, we set $r_s = 0.6$, $\epsilon = 0.2$, $\beta = 0.01$ and $\delta = 0.01$, which are typical values for large tokamak plasmas. Transport coefficients are chosen as $\mu = 10^{-5}$, $\eta_\parallel = 10^{-5}$, $\eta_\perp = 2\times10^{-5}$, $\chi_\parallel = 1$ and $\chi_\perp = 10^{-5}$, where these coefficients include anomalous effects due to turbulent transports (hyper viscosities). Equations are solved with a spectral expansion in the poloidal and the toroidal direction using the poloidal mode number m and the toroidal mode number n. For simplicity, we consider only resonant modes on the $q = 2$ resonant surface, which satisfy the relation $m/n = 2$ (single helicity). For the above parameters, the initial Δ' value for $(m, n) = (2, 1)$ is $\Delta'_{2,1} = 17.8$, so that $(2, 1)$ is an only unstable mode, while other higher modes are linearly stable. Basically, each perturbation (including the vorticity $\nabla_\perp^2\tilde{\phi}$ and the current $\tilde{j}_\parallel$) $\tilde{f}_{m,n}(r,t)$ satisfies boundary conditions: $\tilde{f}_{m,n}(0) = \tilde{f}_{m,n}(1) = 0$ for $m, n \neq 0$ and $\partial\tilde{f}_{0,0}(0,t)/\partial r| = \tilde{f}_{0,0}(1,t) = 0$, where the center and the edge of the plasma correspond to $r = 0$ and $r = 1$, respectively. The error field (external symmetry-breaking magnetic perturbation) is taken into account by means of changing the edge boundary of the $(2, 1)$ vector potential amplitude such that $\tilde{A}_{2,1}(1) = \psi_a$, where $m\psi_a$ corresponds to an error field strength $|B_r/B_0|$. In the numerical simulations, error field is induced as $\psi_a = 0$ $(0 \le t \le 10000)$ and $\psi_a = 2.5 \times 10^{-4}$ $(10000 \le t)$. For the spectral resolution, $-4 \le n \le 4$ Fourier modes are used, which are enough to resolve the nonlinear dynamics of the drift-tearing mode [8].

2.3 Simulation results

We briefly outline the numerical simulation using Eqs.(1)-(4) (See Ref. [9] for details). In the simulation, small perturbations are initially given, and the linearly unstable drift-tearing mode is excited with an exponential growth. When the magnetic island width overcomes the resistive layer width, a nonlinear growth phase is started. In the nonlinear growth phase, the macroscopic $(0, 0)$ electrostatic potential (radial electric field) with the $(2, 1)$ perturbation (and small but finite $(4, 2)$, $(6, 3)$ and $(8, 4)$ perturbations) are excited by the magnetic island. In the excitation of the $(0, 0)$ electrostatic potential, both the Reynolds stress and the Maxwell stress ($J\times B$ force) by the magnetic island play important roles. The growth of the magnetic island is saturated at $t = 8000$, and stresses by the magnetic island are balanced with a viscous force by the ion viscosity. In this phase, the first nonlinear saturation state is reached. Figure 1 (a) shows a contour of the electrostatic potential at the first nonlinear saturation state ($t = 10000$). A concentric structure due to the $(0, 0)$ component is observed in the whole region, and magnetic island like structures are radially located around $r = 0.6$. After $t = 10000$, the error

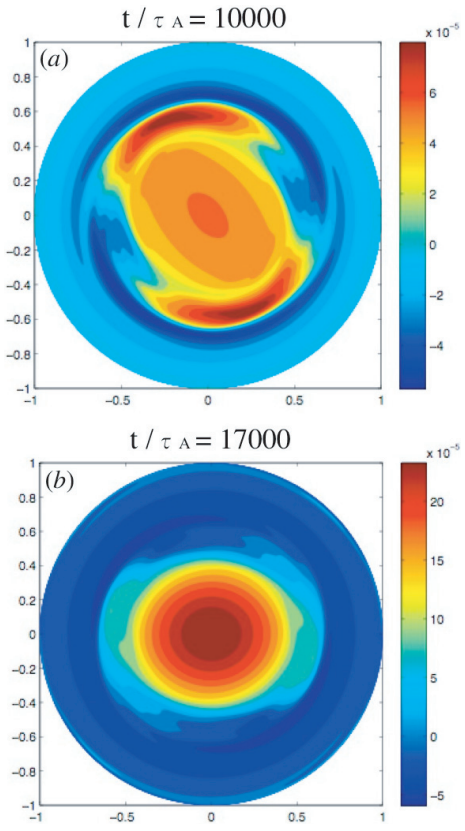

Fig. 1 Simulation results of the electrostatic potential perturbed by the magnetic island (a) before applying the error field and (b) after applying the error field.

field is applied. The magnetic island width is not strongly modified by the error field (a few percent). On the other hand, the electrostatic potential is strongly perturbed by an electromagnetic force due to the interaction between the magnetic island and the error field. Because of the change of the electrostatic potential, the magnetic island rotation is finally locked by the error field. After the locking, the second nonlinear saturation state is reached. Figure 1 (b) shows a contour of the electrostatic potential at the second nonlinear saturation state ($t = 17000$). In comparison with the first saturation state, the structure of the electrostatic potential is strongly modified, and the concentric structure becomes dominant.

3. Numerical Diagnostics

3.1 Numerical heavy ion beam probe

In experimental observations [10], the basic mechanism of the HIBP is the following: (i) a focused singly-ionized heavy ion beam is injected into magnetized plasmas, (ii) heavy ions move under the electromagnetic force by magnetized plasmas, (iii) some heavy ions are doubly-ionized due to the interaction with plasma particles, and (iv) doubly-ionized heavy ions are detected after coming out from plasmas. The electrostatic potential at the ionization point is calculated by a difference between kinetic energies of heavy ions at the injection point with those at the detecting point.

We have developed a module which simulates the HIBP measurement system. The fluctuating electrostatic potential is measured by combining this module with various nonlinear simulation codes. In our numerical HIBP module, an equation of motion is solved to obtain trajectories of heavy ions on the plasma fields. Since the velocity of heavy ion ($\sim$ Alfvén velocity) is much faster than that of the fluid plasma motion, the trajectory calculation is performed in each snap shot of simulation fields. Feedback effects of the HIBP on plasma fields is out of scope in the present scheme, and the influence of the divergence of the beam is neglected, for simplicity. According to the HIBP in experiments, the finite beam width is considered, which gives rise to a spacial resolution. Possible trajectories from the injection point to the detecting point are taken into account so as to quantitatively evaluate an effect of the finite beam width.

Figure 2 shows trajectories of heavy ions calculated by the numerical HIBP module at $t = 10000$. According to experiments [10], gold ions (Au^+) with 6.0 MeV at the injection point are considered, and the ambient magnetic field, the major radius and the equilibrium plasma density are chosen such that $B_0 = 1.0\,\mathrm{T}$, $R_0 = 350\,\mathrm{cm}$ and $n_0 = 3.0 \times 10^{13}\,\mathrm{cm}^{-3}$, respectively. In the numerical simulation, $\epsilon = 0.2$ is considered, therefore minor radius is $a = 70\,\mathrm{cm}$. Beam widths at the injection and detecting points are also independent parameters. In the present case, beam widths at both side are chosen to be 2×10^{-2}

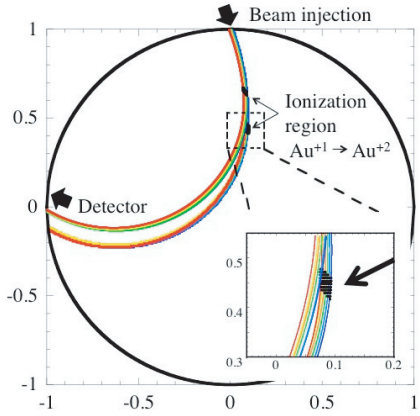

Fig. 2 Trajectories of heavy ions given by the numerical HIBP module. Ionization points are shown by black dots.

times minor radius, i.e. 1.4 cm. In Fig. 2, two detecting positions are selected, and the perturbed electrostatic potential in two different ionization regions are obtained. The inner and the outer ionization regions in Fig. 2 are located near the inner and outer separatrixes of magnetic island, respectively.

A mean value of the electrostatic potential is given by its ensemble average in an ionization region (i.e, an average of electrostatic potentials at black dots in Fig. 2). An error bars of the observed value due to the finite ionization region is calculated by the standard deviation of the mean. The radial resolution is typically the same order as the beam width.

3.2 Measurement of perturbed electrostatic potential

Using the numerical HIBP module, the perturbed electrostatic potential given by the numerical simulation in the previous section is measured. In the following analyzes, the normalization parameter of the electrostatic potential is given by $B_0 a^2/c\tau_A = 8.8 \times 10^2\,\mathrm{kV}$, and that of the time is $\tau_A = 0.88\,\mu\mathrm{s}$ in the present parameters.

Figure 3 shows time evolutions of the electrostatic potential in the vicinity of the (a) inner ($r = 0.46 \pm 0.01$) and (b) outer ($r = 0.65 \pm 0.01$) separatrixes of the magnetic island. The excitation of the electrostatic potential by the magnetic island and the influence of the error field are clearly observed. In these figures, the error bar strongly changes in time.

The radial profile of the electrostatic potential is obtained by the multipoint measurement. Fifty detecting points are considered and the whole radial range is measured (in experiments, the measurement is limited in the plasma core region). Corresponding to Fig. 1, Fig. 4 shows the radial profile of the electrostatic potential at the (a) first and (b) second nonlinear saturation state. In Fig. 4 (a), the steep radial gradient is observed in the vicinity of magnetic island ($r \sim 0.6$), which indicates that the radial elec-

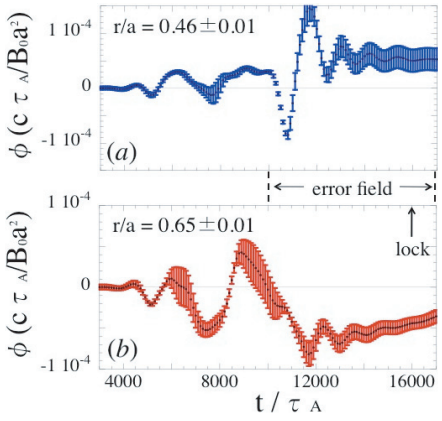

Fig. 3 Time evolutions of the electrostatic field measured by the numerical HIBP module.

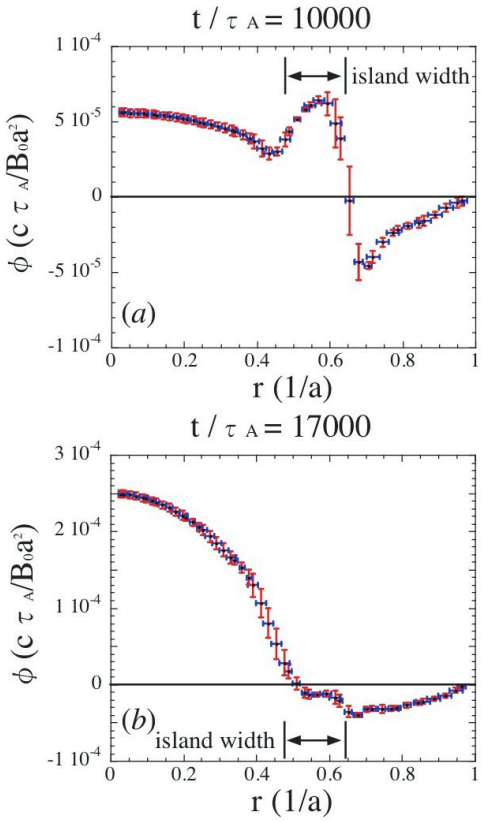

Fig. 4 Radial profiles of the electrostatic field measured by the numerical HIBP module.

tric field ($\sim$ 1 kV/m) is generated inside the island. In this regime, a scale length of the radial gradient, $(\partial_r\phi/\phi)^{-1}$, is comparable to or smaller than the beam width, which gives rise to large measurement errors. In the second saturation state, in Fig. 4 (b), the radial profile of electrostatic potential is globally changed. In the vicinity of the outer separatrix, the radial gradient is moderated, and simultaneously error bars become smaller. On the other hand, the increase of error bars near the inner separatrix is associated with the radial gradient steepening. Therefore, it is concluded that the fluctuation of the error bar observed in Fig. 3 is due to the change in the radial gradient of the electrostatic potential.

4. Summary

Nonlinear dynamics of magnetic islands is simulated, and the numerical diagnostics of the electrostatic potential perturbed by the islands is performed. The excitation of the electrostatic potential by the magnetic island is observed. A module simulating the heavy ion beam probe (HIBP) is introduced, which plays a role of a filter for translating the simulation data into the observable data in experiments. Using this module, time evolutions and spatial profiles of the electrostatic potential are successfully measured. In particular, the spatial resolution and the error bar due to the finite width of the beam is evaluated. It is found that the finite beam width gives rise to large error bars in the region where the radial scale length of the electrostatic potential is comparable to the beam width.

In future works, we combine the numerical HIBP module with turbulence codes, for which the spacial resolution of HIBP is more important.

Acknowlegements

The authors would like to thank Prof. K. Ida for his useful discussions. This work is partially supported by a Grant-in-Aid for Scientific Research (S) (21224014) and (B) (19360415, 19360418). We also acknowledge the collaboration program of the Research Institute for Applied Mechanics of Kyushu University and the National Institute for Fusion Science, Japan (NIFS09KDAD009, NIFS09KTAD009).

[1] F. L. Waelbroeck, Nucl. Fusion **49**, 104025 (2009).
[2] K. Ida *et al*, Phys. Rev. Lett. **11**, 015002 (2002).
[3] Bruce D. Scott, A. B. Hassam and J. F. Drake, Phys. Fluids **28**, 275 (1985).
[4] M. Ottaviani, F. Porcelli and D. Grasso, Phys. Rev. Lett. **13**, 075001 (2004).
[5] S. Nishimura, S. Benkadda, M. Yagi, S.-I. Itoh and K. Itoh, Phys. Plasmas **15**, 092506 (2008).
[6] N. Kasuya, M. Yagi, S.-I. Itoh and K. Itoh, Phys. Plasmas **15**, 052302 (2008).
[7] T. Yamada, S.-I. Itoh, T. Maruta, N. Kasuya, Y. Nagashima, S. Shinohara, K. Terasaka, M. Yagi, S. Inagaki, Y. Kawai, A. Fujisawa and K. Itoh, Nature Phys. **4**, 721 (2008).
[8] S. Nishimura, M. Yagi, S.-I. Itoh and K. Itoh, J. Phys. Soc. Jpn. **77**, 014501 (2008).
[9] S. Nishimura, M. Yagi, K. Itoh, S.-I. Itoh and S. Benkadda, 'Locking of magnetic island rotation by static error field', Nucl. Fusion (in press).
[10] T. Ido *et al*, Plasma Science and Technology **11**, 460 (2009).